ACS APPLIED MATERIALS & INTERFACES

Research Article

www.acsami.org

Microscopic Investigation of Grain Boundaries in Organolead Halide Perovskite Solar Cells

Jiang-Jun Li, Jing-Yuan Ma, Qian-Qing Ge, Jin-Song Hu, Dong Wang,* and Li-Jun Wan*

Beijing National Laboratory for Molecular Science, Key Laboratory of Molecular Nanostructure and Nanotechnology, Institute of Chemistry, Chinese Academy of Sciences, Beijing 100190, P. R. China

Supporting Information

ABSTRACT: Grain boundaries (GBs) play an important role in organic−inorganic halide perovskite solar cells, which have generally been recognized as a new class of materials for photovoltaic applications. To definitely understand the electrical structure and behavior of GBs, here we present Kelvin probe force microscopy and conductive atomic force microscopy (c-AFM) measurements of both typical and inverted planar organolead halide perovskite solar cells. By comparing the contact potential difference (CPD) of these two devices in the dark and under illumination, we found that a downward band bending exists in GBs that predominantly attract photoinduced electrons. The c-AFM measurements observed that higher photocurrents flow through GBs when a low bias overcomes the barrier created by the band bending, indicating that GBs act as effective charge dissociation interfaces and photocurrent transduction pathways rather than recombination sites.

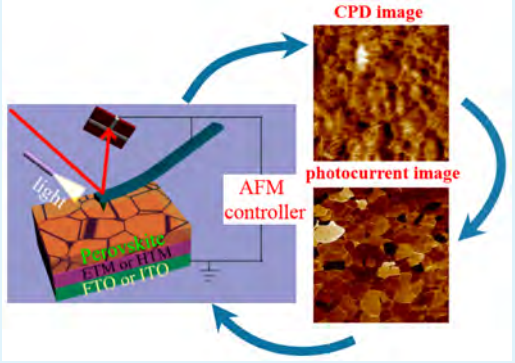

KEYWORDS: *perovskite solar cells, GBs, KPFM, c-AFM, CPD, photocurrent*

INTRODUCTION

Organolead halide perovskites have recently emerged as a new and promising class of materials for photovoltaic applications. In the past few years, there has been a swift surge on perovskite solar cells because of their low cost and superb photovoltaic performance. So far, power conversion efficiencies (PCEs) have increased from 3.8%[1] to recently certified 20.1%.[2] The superb performance on an organolead halide perovskite solar cell can be attributed to its high absorption coefficient at the visible-light range, optimum band gap, ambipolar carrier transportation properties, and high charge carrier mobility of 20 $cm^2/V{\cdot}s$.[3−8] Dong et al. reported that electron−hole diffusion lengths of perovskite single crystals exceed 175 μm,[9] which is much higher than that of a typical organic solar cell and a dye-sensitized solar cell. A typical perovskite solar cell adopts a thin-film p−i−n structure with metallic oxide mesoporous layers (TiO_2, ZnO, and NiO) as electron-transport materials on a compact TiO_2 cathode and polymers as hole-transport materials. For this structure, photogenerated carrier transport in the perovskite layer is followed by electron separation at n-type metallic oxide/perovskite interfaces and by hole separation at p-type polymer/perovskite interfaces. Currently, another typical perovskite solar cell with a simple planar heterojunction p−i−n architecture without a mesoporous metal oxide layer has also been investigated. These structures are featured by sandwiching the perovskite layer between electrode buffer layers and have achieved PCEs of 13.1−17.2%.[10−15]

Great efforts have been made to develop synthetic methods for the perovskite active layer, such as spin coating,[16,17] coevaporation,[18,19] vapor-assisted depositions,[20] and postsynthesis treatment, to control the chemical composition, crystalline morphology, and coverage of active materials. Generally, the perovskite active layer is polycrystalline in nature, and there are a large number of grain boundaries (GBs) in the thin film. Crystal defects and impurities in the GBs can lead to the formation of localized energy states in the band gap. These in-gap states may act as recombination sites and can capture carriers from bulk material and decrease the photocurrent. On the other hand, the unbalanced energy state between the GBs and bulk material gives rise to band bending, which may help the spatial separation of photogenerated electron−hole pairs and facilitate channeling of the carriers along the GBs. Investigation of the electronic properties of GBs is crucial for understanding the performance of the perovskite solar cell and rational design of active-layer structures.

The existence of GBs is a general observation for thin-film inorganic solar cells. Numerous studies have now shown that GBs in CdTe, $Cu_2ZnSn(Se,S)_4$, and $Cu(In,Ga)Se_2$ thin-film solar cells are electrically benign and beneficial to the performance.[21−29] It is suggested that a higher surface potential at the GBs in these solar cells forms downward band bending and a built-in potential at the GBs. This built-in potential creates a barrier that repels holes and attracts electrons (minority carriers). Thus, photogenerated electrons can easily

Received: October 14, 2015
Accepted: December 3, 2015
Published: December 3, 2015

DOI: 10.1021/acsami.5b09801
ACS Appl. Mater. Interfaces 2015, 7, 28518−28523

be repelled out of the regime through the conduction bend of the GBs, which results in suppression of the recombination rate of the carriers. So far, few groups have investigated the electrical and optoelectrical properties of GBs in organic−inorganic perovskite polycrystalline solar cells. Edri et al.[30] reported that a higher work function at the GBs, which indicates that a small potential barrier at the GB hinders electron transport between grains, is reduced under illumination. Chen et al.[31] reported that by moderate postannealing, a higher surface potential of 50 mV at the GBs changes to a lower surface potential of 30 mV. Moderate postannealing gives rise to the PbI_2 phase, which changes the grain to the GB bending from downward to upward, which contributes to the reduction of the combination between layers. On the other hand, Yun et al.[32] reported that, in a $CH_3NH_3PbI_3/TiO_2$ heterojunction device, the contact potential difference (CPD) at the GBs is lower than that in the grain interior in the dark and becomes higher than that in the grain interior under illumination. Also, conductive atomic force microscopy (c-AFM) measurement shows a higher short-circuit current near the GBs than the grain interior. Kim et al.[33] discovered that, for $CH_3NH_3Pb(I_{0.88},Br_{0.12})_3$, there are a higher surface potential (150 mV) at the GBs and a lower current flow through the GBs than through grains in dark conditions, while the GBs on the $CH_3NH_3PbI_3$ film show a higher surface potential of only 50 mV. In view of the debate on the band bending at GBs in these rare reports, it is critically important to exploit the electronic properties of the GBs and their effect on the photogenerated carrier behavior.

In this paper, we use Kelvin probe force microscopy (KPFM) and c-AFM to study the band structure and photoelectric behavior of GBs in organic−inorganic halide perovskite films. By measuring the surface potential and conductivity at nanoscale, KPFM and c-AFM can provide useful insight into understanding the localized band structures in organic or inorganic solar cells. As shown in Figure 1, we have carried out

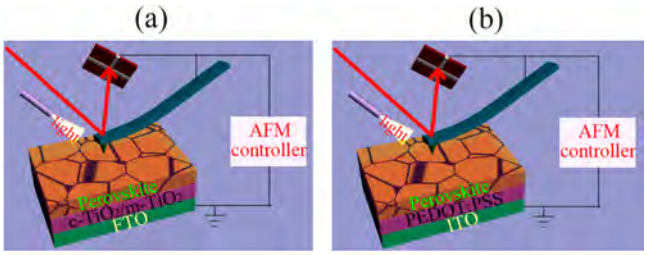

Figure 1. Illustration of the AFM setups and device structures of (a) the mesoporous $CH_3NH_3PbI_3/m\text{-}TiO_2/c\text{-}TiO_2/FTO$ and (b) the inverted nonmesoporous $CH_3NH_3PbI_3/PEDOT:PSS/ITO$ planar heterojunction.

comparative local photoelectrical characterizations on mesoporous $FTO/c\text{-}TiO_2/m\text{-}TiO_2/CH_3NH_3PbI_3$ typical devices and inverted nonmesoporous $ITO/PEDOT:PSS/CH_3NH_3PbI_3$ planar devices. Because mesoporous TiO_2 and PEDOT:PSS act as hole- and electron-blocking layers in solar cell devices, respectively, such a comparative study is expected to provide important insight about the effect of GBs on electron and hole transportation.

RESULTS AND DISCUSSION

Surface Potential Measurement of Perovskite Devices by KPFM. We first fabricated a typical perovskite solar cell structure, $CH_3NH_3PbI_3/m\text{-}TiO_2/c\text{-}TiO_2/FTO$. Figure 2 shows the topography and surface potential images of the perovskite film. The change of the CPD value reflects the change of the work function of the local sample surface, and the brighter region has a higher work function. From topography mapping, we can see the grains of $CH_3NH_3PbI_3$ with diameters ranging from 50 to 300 nm. The absolute surface work function of $CH_3NH_3PbI_3$ grains in the dark (in Figure 2b) is calculated to be about ∼4.8 eV, which is consistent with previous literature.[34] From the CPD image in dark conditions, one sees that the CPD on the GB is higher than that on the grain, indicating that positively charged GBs form downward band bending in the space charge region around the GBs, which is consistent with previous literature.[30,31,33] This downward band bending is between 20 and 80 meV and makes a low barrier for holes.

Figure 2c shows the CPD distribution of the same area under illumination. As indicated on the same scale bar, the average CPD over the surface of the perovskite under illumination is ∼100 mV higher than that in the dark. This observation suggests that holes accumulate in the perovskite layer, while electrons transport to the electron-transport material TiO_2 and finally transport to the ground. Furthermore, the CPD cross-sectional profile along the white lines marked in Figure 2a−c is reproduced in Figure 2d. The CPD difference between the GB and grains is unchanged under illumination, which indicates the ability of hole capture at GBs is comparable to that at grains.

Because the downward band bending at GBs is supposed to attract electrons, it is significant to investigate the role of GBs in electron separation and collection. We then fabricated a planar heterojunction device, $CH_3NH_3PbI_3/PEDOT:PSS/ITO$, which is inverted compared to the typical perovskite device. Contrary to the hole-blocking nature of TiO_2, PEDOT:PSS is an electron-blocking layer, which allows the transportation of holes freely. Figure 3 shows the topography and surface potential images of the inverted planar heterojunction device. From topography mapping, we can see the uniform polycrystalline grains of $CH_3NH_3PbI_3$ with diameters ranging from 100 to 400 nm. As shown in Figure 3b, we also found that the CPD on the GB is higher than that on the grain in dark conditions. The similar result further demonstrates downward band bending in the space charge region around the GBs. It is worth noting that not all of the GBs exhibit marked higher CPD. Such an observation suggests that the electrical properties of GBs may be strongly related to the interface of neighboring grains.

The band bending at the GBs of the planar heterojunction device is between 100 and 300 meV and is higher than that of a typical device. Figure 3c shows CPD mapping under illumination of the same area. When Figure 3b is compared with Figure 3c, the darkened CPD image under illumination indicates that electrons are accumulated on the perovskite surface, which agrees with the electron-blocking behavior of PEDOT:PSS. To display the contrast better, a line profile along the white line in the topography and CPD images is depicted in Figure 3d. It is obviously found that, under illumination, the CPD around the GBs decreases by about −350 mV, which is much lower than that on grains (about −200 mV), suggesting that more photoinduced electrons are accumulated at the GBs. The electron attraction at the GBs can be attributed to the downward band bending. Combined with the aforementioned typical device measurements, it shows that GBs predominantly attract electrons in the photovoltaic process.

Photocurrrent Measurement of Perovskite Devices by c-AFM. To further understand carrier transportation around the GBs, we used c-AFM to measure the local current on grains

DOI: 10.1021/acsami.5b09801
ACS Appl. Mater. Interfaces 2015, 7, 28518−28523

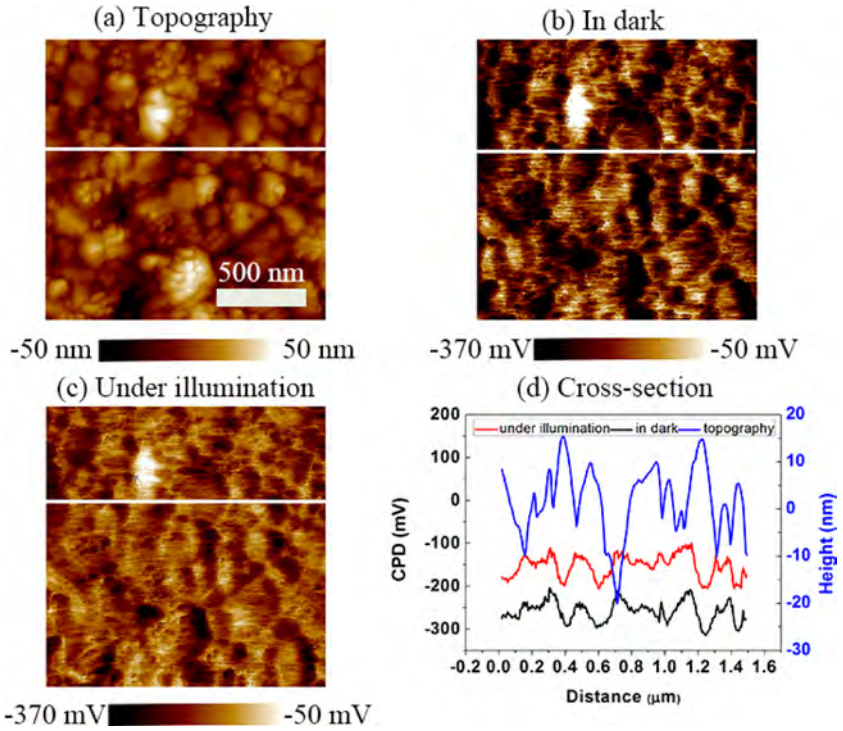

Figure 2. (a) AFM topographic image of the $CH_3NH_3PbI_3$/m-TiO_2/c-TiO_2/FTO typical device. Corresponding CPD images recorded (b) in the dark and (c) under illumination. (d) CPD variation along the white lines marked in parts a−c.

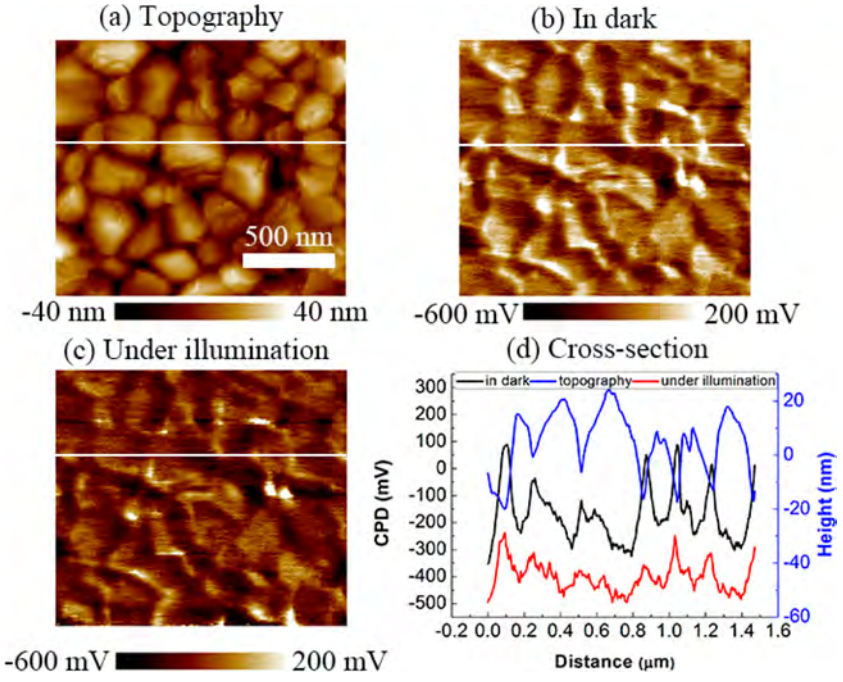

Figure 3. (a) AFM topographic image of the $CH_3NH_3PbI_3$/PEDOT:PSS/ITO planar heterojunction device. Corresponding CPD images recorded (b) in the dark and (c) under illumination. (d) CPD variation along the white lines marked in parts a−c.

and GBs and thus determine the surface conductivity. First, we performed c-AFM on a typical perovskite device. In Figure 4b, we show the results from c-AFM measurements under steady illumination on $CH_3NH_3PbI_3$ without a sample bias voltage. A positive photocurrent flows through the grains with an average magnitude of 16 pA, while nearly zero current was detected on the GBs. We then applied a low positive sample bias of 0.3 V. The corresponding topographic image in which the grains and GBs are clearly seen is presented in Figure 4c. As can be seen in Figure 4d, at this low bias, the photocurrents increase dramatically to the average magnitude of 129 pA and are much higher at the GBs than at the grains.

We also performed the c-AFM measurements at negative sample bias but obtained negligible current, indicating the diode characteristics of the device (a typical $I-V$ curve is shown in Figure S1 in the Supporting Information). The different

DOI: 10.1021/acsami.5b09801
ACS Appl. Mater. Interfaces 2015, 7, 28518−28523

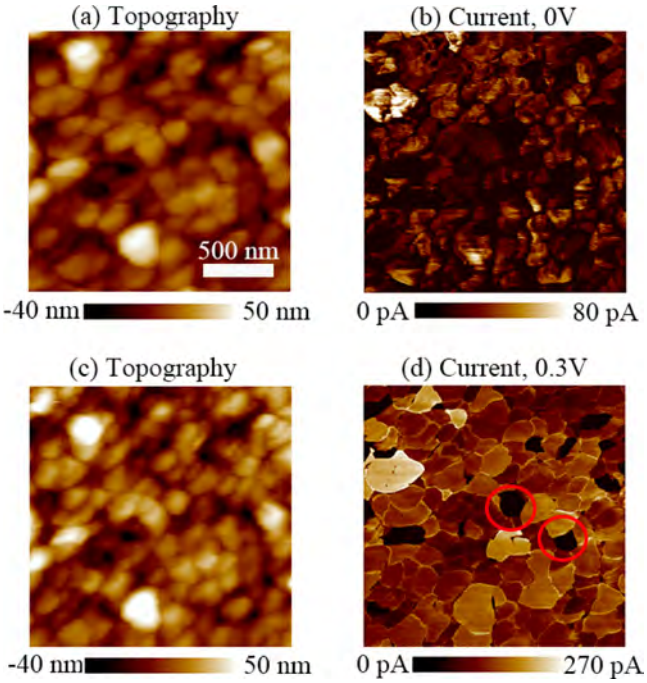

Figure 4. (a and c) AFM topographic images of a $CH_3NH_3PbI_3$/m-TiO_2/c-TiO_2/FTO typical device. (b and d) Corresponding current images recorded under illumination with 0 and 0.3 V, respectively.

electric properties between GBs and grain help us to understand the fundamental conduction processes in the device. First, the mobility is not expected to vary significantly with the bias voltage and is likely to be higher in the grains than at and near the GBs because of defects or dislocations at the GBs. Second, as from the KPFM measurements, the downward band bending at the GBs repels holes and creates a built-in barrier for charge transportation. At low sample bias, the carrier-transport process is more effective on the grains than at the GBs. However, once a positive bias is applied to overcome the barrier at the GBs, intergrain carrier transport becomes possible. The effective carrier correlated to the photocurrents at the GBs comes from the bulk grains. The higher photocurrent at the GBs at high sample bias suggests that the GBs act as channels for current to flow rather than recombination sites. We ascribe the efficient charge transfer to elimination of the barrier by external electric-field compensation of the band bending, as indicated by the green arrow in Figure 5. The threshold voltage can be observed from the $I-V$ curve in Figure S1 in the Supporting Information. It is worth noting that the grains with poor conductivity, as depicted by the red circles in Figure 4d, may correspond to the PbI_2 phase generated during the annealing process.[31]

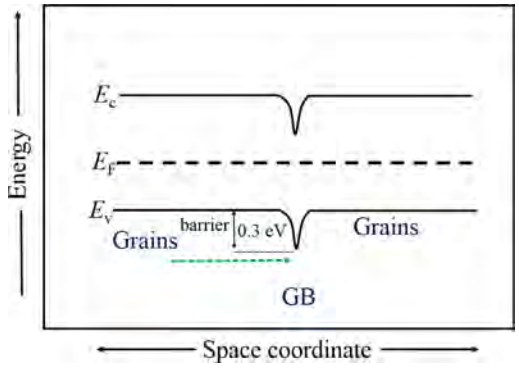

Figure 5. Band alignment between grains and GBs.

Finally, we performed c-AFM measurements on the planar heterojunction device $CH_3NH_3PbI_3$/PEDOT:PSS/ITO, as depicted in Figure 6. The corresponding topographic image in which the grains and GBs are clearly seen is presented in Figure 6a. Under illumination and without sample bias, the photocurrents are always negative and the average magnitude is −14 pA, which is opposite to the case of a typical device, as can be seen in Figure 6b. Similarly, there is no noticeable photocurrent observed through GBs. We then applied a low negative sample bias of −0.3 V. As shown in Figure 6c, at this low bias, the photocurrents through grains increase dramatically to the average magnitude of −133 pA. Moreover, the dark contrasts of the GBs show that the photocurrents through the GBs distinctly exceed those through grains. We also performed c-AFM measurements at relatively low positive sample bias but also obtained negligible current, indicating the diode characteristics of the planar device. Similarly, the threshold voltage when the photocurrents of the GBs surpass those of grains also can be observed from the $I-V$ curve in Figure S2 in the Supporting Information. Our observations can be attributed to the fact that GBs act as both efficient charge dissociation interfaces and channels for current to flow through rather than strong recombination centers. At such a low bias, if GBs act as recombination sites, the photocurrents through the GBs would be much lower than those of the grains or may even be negligible.

The barrier at GB separate carriers is expected to increase the open-circuit voltage (V_{oc}). Meanwhile, the higher photocurrent across the GBs shows that it can improve the short-circuit current density (J_{sc}) but may reduce the open-circuit voltage by creating a shunting path due to decreasing electron−hole carrier recombination. It has been verified that perovskite solar cells with large-scale grains and a perovskite single crystal displayed superior electronic and photovoltaic performances.[9,35] Characterization and modeling attribute the improved performance to high-quality grains with reduced defects and improved carrier mobility. Therefore, both optimizing the grain quality and precisely controlling the GBs (for example, barrier height and resistance) should be considered simultaneously for improvement of the PCEs of the perovskite solar cells.

CONCLUSION

In summary, comparative nanoscale electrical characterizations of both typical and inverted organolead halide perovskite solar cells were carried out by using KPFM and c-AFM. KPFM measurements confirmed that the downward band bending at the GBs thus forms a low barrier which predominantly attracts electron under illumination. c-AFM measurements showed that the photocurrent flows through the GBs are negligible at 0 V bias, while the major photocurrents form on the grains. However, the photocurrents at the GBs become much higher than those of the grains when the bias overcomes the barrier of the GBs. These two measurements demonstrate the enhanced photoinduced electron collections taking place at the GBs that act as effective charge dissociation interfaces and photocurrent transduction pathways. Direct microscopic study of the optoelectronic characterization can help in the understanding of the local properties of photovoltaic materials, which is

DOI: 10.1021/acsami.5b09801
ACS Appl. Mater. Interfaces 2015, 7, 28518−28523

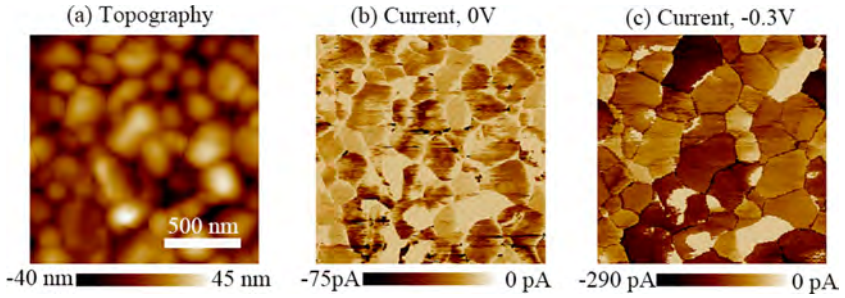

Figure 6. (a) AFM topographic image of the $CH_3NH_3PbI_3$/PEDOT:PSS/ITO planar heterojunction device. (b and c) Corresponding current images recorded under illumination with 0 and −0.3 V, respectively.

pivotally important for device engineering of the organolead halide perovskite solar cell.

EXPERIMENTAL SECTION

The fabrication procedures of two devices can be seen in the Supporting Information. AFM experiments were carried out in a glovebox under an argon atmosphere at room temperature and pressure (Multimode 8, Bruker). All of the measurements were performed in the dark (the glovebox was covered with light-blocking curtains) and under continuous visible-light (400−800 nm) illumination at an angle of ∼45°, so the probe does not block the incident light. Irradiation was provided by a commercial Sun Full Spectrum Light Source (NBet, Beijing) optical fiber at 20 mW/cm^2, which is well matched with the natural spectrum in the range of visible light. Estimated irradiation power levels at the sample surface were about 14 mW/cm^2. It is worth a reminder that the AFM laser has a wavelength of above 600 nm (E > 2.07 eV). However, the intensity of the laser is low and does not significantly affect our measurements.

In our frequency-modulation KPFM (FM-KPFM), the first scan is used for topographic imaging with peak force mode, and then the probe is lifted in interleave mode and measures the CPD. The frequency modulation (f_{mod}) applied to the tip is about 2 kHz. A silicon probe coated with gold (NSG03/Au, NT-MDT) with a force constant of ∼0.4−1.2 N/m and a tip radius of ∼12 nm was used for CPD measurement with the lift mode.

c-AFM measurements were performed in contact mode using the same conductive probe coated with gold to record the current between the sample and tip when a bias voltage was applied to the sample.

ASSOCIATED CONTENT

Supporting Information

The Supporting Information is available free of charge on the ACS Publications website at DOI: 10.1021/acsami.5b09801.

Pretreatment of glass electrodes, synthesis methods of c-TiO_2, m-TiO_2, the PEDOT:PSS layer, and the perovskite active layer, I−V curves for a $CH_3NH_3PbI_3$/m-TiO_2/c-TiO_2/FTO typical device and a $CH_3NH_3PbI_3$/PEDOT:PSS/ITO planar heterojunction device (PDF)

AUTHOR INFORMATION

Corresponding Authors

*E-mail: wangd@iccas.ac.cn.
*E-mail: wanlijun@iccas.ac.cn.

Funding

This work was supported by the National Key Project on Basic Research (Grant 2012CB932902), National Natural Science Foundation of China (Grants 21127901, 21233010, 21433011, and 21373236), and Strategic Priority Research Program of the Chinese Academy of Sciences (Grant XDB12020100).

Notes

The authors declare no competing financial interest.

ABBREVIATIONS

c-AFM, conductive atomic force microscopy
CPD, contact potential difference
GB, grain boundary
J_{sc}, short-circuit current density
KPFM, Kelvin probe force microscopy
PCE, power conversion efficiency
V_{oc}, open-circuit voltage

REFERENCES

(1) Kojima, A.; Teshima, K.; Shirai, Y.; Miyasaka, T. Organometal Halide Perovskites as Visible-Light Sensitizers for Photovoltaic Cells. *J. Am. Chem. Soc.* **2009**, *131* (17), 6050−6051.
(2) Green, M. A.; Emery, K.; Hishikawa, Y.; Warta, W.; Dunlop, E. D. Solar Cell Efficiency Tables (Version 45). *Prog. Photovoltaics* **2015**, *23* (1), 1−9.
(3) Kazim, S.; Nazeeruddin, M. K.; Grätzel, M.; Ahmad, S. Perovskite as Light Harvester: A Game Changer in Photovoltaics. *Angew. Chem., Int. Ed.* **2014**, *53*, 2812−2824.
(4) Snaith, H. J. Perovskites: The Emergence of a New Era for Low-Cost, High-Efficiency Solar Cells. *J. Phys. Chem. Lett.* **2013**, *4*, 3623−3630.
(5) Boix, P. P.; Nonomura, K.; Mathews, N.; Mhaisalkar, S. G. Current Progress and Future Perspectives for Organic/Inorganic Perovskite Solar Cells. *Mater. Today* **2014**, *17*, 16−23.
(6) Park, N.-G. Organometal Perovskite Light Absorbers. Toward a 20% Efficiency Low-Cost Solid-State Mesoscopic Solar Cell. *J. Phys. Chem. Lett.* **2013**, *4*, 2423−2429.
(7) Kim, H.-S.; Im, S. H.; Park, N.-G. Organolead Halide Perovskite: New Horizons in Solar Cell Research. *J. Phys. Chem. C* **2014**, *118*, 5615−5625.
(8) Oga, H.; Saeki, A.; Ogomi, Y.; Hayase, S.; Seki, S. Improved Understanding of the Electronic and Energetic Landscapes of Perovskite Solar Cells: High Local Charge Carrier Mobility, Reduced Recombination, and Extremely Shallow Traps. *J. Am. Chem. Soc.* **2014**, *136*, 13818−13825.
(9) Dong, Q.; Fang, Y.; Shao, Y.; Mulligan, P.; Qiu, J.; Cao, L.; Huang, J. Electron-Hole Diffusion Lengths> 175 mm in Solution-Grown $CH_3NH_3PbI_3$ Single Crystals. *Science* **2015**, *347*, 967−970.
(10) Wang, X.; Li, X.; Tang, G.; Zhao, L.; Zhang, W.; Jiu, T.; Fang, J. Improving Efficiency of Planar Hybrid $CH_3NH_3PbI_{3-x}Cl_x$ Perovskite Solar Cells by Isopropanol Solvent Treatment. *Org. Electron.* **2015**, *24*, 205−211.
(11) Liu, X.; Yu, H.; Yan, L.; Dong, Q.; Wan, Q.; Zhou, Y.; Song, B.; Li, Y. Triple Cathode Buffer Layers Composed of PCBM, C_{60}, and LiF for High-Performance Planar Perovskite Solar Cells. *ACS Appl. Mater. Interfaces* **2015**, *7*, 6230−6237.
(12) Kuang, C.; Tang, G.; Jiu, T.; Yang, H.; Liu, H.; Li, B.; Luo, W.; Li, X.; Zhang, W.; Lu, F.; Fang, J.; Li, Y. Highly Efficient Electron Transport Obtained by Doping PCBM with Graphdiyne in Planar-

Heterojunction Perovskite Solar Cells. *Nano Lett.* **2015**, *15*, 2756−2762.
(13) Qian, M.; Li, M.; Shi, X. B.; Ma, H.; Wang, Z. K.; Liao, S. L. Planar Perovskite Solar Cells with 15.75% Power Conversion Efficiency by Cathode and Anode Interfacial Modification. *J. Mater. Chem. A* **2015**, *3*, 13533−13539.
(14) Heo, J. H.; Han, H. J.; Kim, D.; Ahn, T. K.; Im, S. H. Hysteresis-Less Inverted $CH_3NH_3PbI_3$ Planar Perovskite Hybrid Solar Cells with 18.1% Power Conversion Efficiency. *Energy Environ. Sci.* **2015**, *8*, 1602−1608.
(15) Chiang, C.-H.; Tseng, Z.-L.; Wu, C.-G. Planar Heterojunction Perovskite/PC71BM Solar Cells with Enhanced Open-Circuit Voltage via a(2/1)-Step Spin-Coating Process. *J. Mater. Chem. A* **2014**, *2*, 15897−15903.
(16) Huang, F.; Dkhissi, Y.; Huang, W.; Xiao, M.; Benesperi, I.; Rubanov, S.; Zhu, Y.; Lin, X.; Jiang, L.; Zhou, Y. Gas-Assisted Preparation of Lead Iodide Perovskite Films Consisting of a Monolayer of Single Crystalline Grains for High Efficiency Planar Solar Cells. *Nano Energy* **2014**, *10*, 10−18.
(17) Xiao, M.; Huang, F.; Huang, W.; Dkhissi, Y.; Zhu, Y.; Etheridge, J.; Gray-Weale, A.; Bach, U.; Cheng, Y. B.; Spiccia, L. A Fast Deposition-Crystallization Procedure for Highly Efficient Lead Iodide Perovskite Thin-Film Solar Cells. *Angew. Chem.* **2014**, *126* (37), 10056−10061.
(18) Liu, M.; Johnston, M. B.; Snaith, H. J. Efficient Planar Heterojunction Perovskite Solar Cells by Vapour Deposition. *Nature* **2013**, *501*, 395−398.
(19) Malinkiewicz, O.; Yella, A.; Lee, Y. H.; Espallargas, G. M.; Graetzel, M.; Nazeeruddin, M. K.; Bolink, H. J. Perovskite Solar Cells Employing Organic Charge-Transport Layers. *Nat. Photonics* **2013**, *8*, 128−132.
(20) Chen, Q.; Zhou, H.; Hong, Z.; Luo, S.; Duan, H. S.; Wang, S. H.; Liu, Y. S.; Li, G.; Yang, Y. Planar Heterojuction Perovskite Solar Cells via Vapor-Assisted Solution Process. *J. Am. Chem. Soc.* **2014**, *136*, 622−625.
(21) Visoly-Fisher, I.; Cohen, S. R.; Ruzin, A.; Cahen, D. How Polycrystalline Devices Can Outperform Single-Crystal Ones: Thin CdTe/CdS Solar Cells. *Adv. Mater.* **2004**, *16* (11), 879−883.
(22) Kim, G. Y.; Jeong, A. R.; Kim, J. R.; Jo, W.; Son, D.-H.; Kim, D.-H.; Kang, J.-K. Surface Potential on Grain Boundaries and Intragrains of Highly Efficient $Cu_2ZnSn(S, Se)_4$ Thin-Films Grown by Two-Step Sputtering Process. *Sol. Energy Mater. Sol. Cells* **2014**, *127*, 129−135.
(23) Hafemeister, M.; Siebentritt, S.; Albert, J.; Lux-Steiner, M. C.; Sadewasser, S. Large Neutral Barrier at Grain Boundaries in Chalcopyrite Thin Films. *Phys. Rev. Lett.* **2010**, *104* (19), 196602-1−196602-4.
(24) Jiang, C. S.; Repins, I. L.; Beall, C.; Moutinho, H. R.; Ramanathan, K.; Al-Jassim, M. M. Investigation of Micro-Electrical Properties of $Cu_2ZnSnSe_4$ Thin Films Using Scanning Probe Microscopy. *Sol. Energy Mater. Sol. Cells* **2015**, *132* (0), 342−347.
(25) Li, J. B.; Chawla, V.; Clemens, B. M. Investigating the Role of Grain Boundaries in CZTS and CZTSSe Thin Film Solar Cells with Scanning Probe Microscopy. *Adv. Mater.* **2012**, *24*, 720−723.
(26) Jiang, C.-S.; Noufi, R.; Ramanathan, K.; AbuShama, J.; Moutinho, H.; Al-Jassim, M. Does the Local Built-in Potential on Grain Boundaries of Cu (In, Ga) Se_2 Thin Films Benefit Photovoltaic Performance of the Device? *Appl. Phys. Lett.* **2004**, *85* (13), 2625−2627.
(27) Visoly-Fisher, I.; Cohen, S. R.; Cahen, D. Direct Evidence for Grain-Boundary Depletion in Polycrystalline CdTe from Nanoscale Resolved Measurements. *Appl. Phys. Lett.* **2003**, *82*, 556−558.
(28) Yan, Y.; Jiang, C.-S.; Noufi, R.; Wei, S. H.; Moutinho, H. R.; AlJassim, M. M. Electrically Benign Behavior of Grain Boundaries in Polycrystalline $CuInSe_2$ Films. *Phys. Rev. Lett.* **2007**, *99*, 235504-1−235504-4.
(29) Jiang, C.-S; Repins, I. L.; Beall, C.; Moutinho, H. R.; Ramanathan, K.; Al-Jassim, M. M. Investigation of Micro-Electrical Properties of $Cu_2ZnSnSe_4$ Thin Films using Scanning Probe Microscopy. *Sol. Energy Mater. Sol. Cells* **2015**, *132*, 342−347.
(30) Edri, E.; Kirmayer, S.; Henning, A.; Mukhopadhyay, S.; Gartsman, K.; Rosenwaks, Y.; Hodes, G.; Cahen, D. Why Lead Methylammonium Tri-Iodide Perovskite-Based Solar Cells Require a Mesoporous Electron Transporting Scaffold (but Not Necessarily a Hole Conductor). *Nano Lett.* **2014**, *14*, 1000−1004.
(31) Chen, Q.; Zhou, H.; Song, T. B.; Luo, S.; Hong, Z.; Duan, H. S.; Dou, L.; Liu, Y.; Yang, Y. Controllable Self-Induced Passivation of Hybrid Lead Iodide Perovskites toward High Performance Solar Cells. *Nano Lett.* **2014**, *14*, 4158−4163.
(32) Yun, J. S.; Ho-Baillie, A.; Huang, S.; Woo, S. H.; Heo, Y.; Seidel, J.; Huang, F.; Cheng, Y.-B.; Green, M. A. Benefit of Grain Boundaries in Organic−Inorganic Halide Planar Perovskite Solar Cells. *J. Phys. Chem. Lett.* **2015**, *6*, 875−880.
(33) Kim, G. Y.; Oh, S. H.; Nguyen, B. P.; Jo, W.; Kim, B. J.; Lee, D. G.; Jung, H. S. Efficient Carrier Separation and Intriguing Switching of Bound Charges in Inorganic−Organic Lead Halide Solar Cells. *J. Phys. Chem. Lett.* **2015**, *6*, 2355−2362.
(34) Bergmann, V. W.; Weber, S. A. L.; Ramos, F. J.; Nazeeruddin, M. K.; Gratzel, M.; Li, D.; Domanski, A. L.; Lieberwirth, I.; Ahmad, S.; Berger, R. Real-space Observation of Unbalanced Charge Distribution inside a Perovskite-Sensitized Solar Cell. *Nat. Commun.* **2014**, *5*, 5001.
(35) Nie, W.; Tsai, H.; Asadpour, R.; Blancon, J.-C.; Neukirch, A. J.; Gupta, G.; Crochet, J. J.; Chhowalla, M.; Tretiak, S.; Alam, M. A.; Wang, H.-L.; Mohite, A. D. High-efficiency Solution-Processed Perovskite Solar Cells with Millimeter-Scale Grains. *Science* **2015**, *347*, 522−525.

DOI: 10.1021/acsami.5b09801
ACS Appl. Mater. Interfaces 2015, 7, 28518−28523